# Strongly Luminescent Dion-Jacobson Tin Bromide Perovskite Microcrystals Induced by Molecular Proton Donors Chloroform and Dichloromethane

*Shixun Wang, Jasminka Popović, Sanja Burazer, Arsenii Portniagin, Fangzhou Liu, Kam-Hung Low, Zonghui Duan, Yanxiu Li, Yuan Xiong, Yuanming Zhu, Stephen V. Kershaw, Aleksandra B. Djurišić and Andrey L. Rogach**

S. Wang, A. Portniagin, Z. Duan, Dr. Y. Li, Dr. Y. Xiong, Dr. S. V. Kershaw, Prof. A. L. Rogach
Department of Materials Science and Engineering, and Centre for Functional Photonics (CFP), City University of Hong Kong, Hong Kong S.A.R., P. R. China
E-mail: andrey.rogach@cityu.edu.hk

Dr. J. Popović, Dr. S. Burazer
Division of Materials Physics, Laboratory for Synthesis and Crystallography of Functional Materials, Ruđer Bošković Institute, 10000 Zagreb, Croatia

Dr. F. Z. Liu, Prof. A. B. Djurišić
Department of Physics, The University of Hong Kong, Hong Kong S.A.R., P. R. China

Dr. K. H. Low
Department of Chemistry, The University of Hong Kong, Hong Kong S.A.R., P. R. China

Dr. Y. Zhu
SUSTech Academy for Advanced Interdisciplinary Studies, Southern University of Science and Technology of China, Shenzhen, 518055 P. R. China

**Keywords**: Tin-Bromide Perovskites; Dion-Jacobson Structure; Molecular Dopants; Proton Donors; Photoluminescence

**Abstract**: Lead-free two-dimensional perovskites based on tin halide octahedron slabs with Dion-Jacobson (DJ) phases have drawn attention due to their improved stability; still, reports on light-emitting DJ lead-free perovskites are scarce. Herein, a room-temperature ligand assisted re-precipitation method was used to produce $ODASnBr_4$ perovskite microcrystals (ODA denotes protonated 1,8-octanediamine, protonation arising through the addition of HBr). After incorporating molecular dopants chloroform and dichloromethane, not only the crystallinity of the DJ perovskite phase improves, but their emission becomes much stronger due to the formation of hydrogen bonds between $[SnBr_6]^{4-}$ octahedra and acidic C-H proton donors. $ODASnBr_4$ perovskite microcrystals doped with these molecules show a high photoluminescence quantum yield (PLQY) approaching 90%, and their emission remains stable under a continuous ultraviolet irradiation, with less than 10% loss in intensity over 6 hours. Moreover, by tuning the pristine $ODASnBr_4$ with various degrees of exposure to the molecular dopants, the maximum of their self-trapped exciton emission could be fine-tuned over a spectral range of 570-608 nm while maintaining high PLQYs of 83-88%. This provides a convenient way to adjust the spectral position of DJ perovskite emission without changing halides or A-site spacers. Thus, stable and strongly emitting lead-free DJ perovskite materials have been developed.

## Introduction

Metal halide perovskites with a general formulae $ABX_3$, where A = $CH_3NH_3^+$ (methylammonium), $HC(NH_2)_2^+$ (formamidinium), $Cs^+$; B = $Pb^{2+}$, $Ge^{2+}$, $Sn^{2+}$; and X = $I^-$, $Br^-$, $Cl^-$ have been recently considered for a variety of applications, including photovoltaics,[1] light-emitting diodes (LEDs),[2] lasers,[3] photodetectors,[4] and memory (data storage) media.[5] However, their intrinsic ionic nature causes inferior stability against polar solvents, ultraviolet light, and electric fields, which greatly restricts their practical use.[6] Moreover, there is a strong push towards eliminating/substituting their most common toxic ingredient – lead. Demand for stable perovskites has triggered development of their two-dimensional (2D) analogues, which keep the main feature of the perovskite structure where octahedral metal halide units are connected by sharing the corners.[7] The

interlayer spacers between the planes of the octahedra in those 2D perovskites could be either monovalent or divalent long-chain organic cations, which subsequently form two kinds of structures, namely Ruddlesden-Popper (RP) or Dion-Jacobson (DJ) perovskite phases.[8] A wide range of such 2D structures could be generated by adopting different organic spacers and configuring the number of inorganic layers with alternative methylammonium, formamidinium, or Cs ions.[9] Lead-containing 2D perovskite films in the RP phase have already been adopted in both photovoltaics and LEDs.[10] Their lead-free counterparts usually show photoluminescence (PL) originating from self-trapped excitons (STEs) by direct relaxation, or thermal activation and tunneling across a certain level of potential barrier of height $E_b$ that transforms free excitons to STEs (Figure S1).[11] Still, lead-free RP perovskites generally suffer from undesirably low PL quantum yields (QYs) and presently their structural stability issues prevent any practical applications due to their long monovalent organic chains and the weak van der Waals forces across the large gaps between each layer, which reduce material stability and thus impact device performance.[7a, 12]

Offering stronger interactions between the perovskite octahedra layers without such a wide van der Waals gap, shorter-chain organic diamines (with amines on each extremum of the molecule) have emerged as interlayer spacers to structure another, DJ perovskite phase, which provides a stable perovskite framework for improved carrier channels.[12-13] However, to the best of our knowledge there have been no reports so far on luminescent lead-free DJ perovskites. In this work, by combining the widely used ligand assisted reprecipitation (LARP) method and liquid-phase crystallization,[14] we developed a room-temperature synthetic routine to obtain yellow-emitting 2D perovskite microcrystals with a general formula of $ODASnBr_4$ (ODA denotes protonated 1,8-octanediamine). Following the synthetic strategy of the LARP method, dimethylformamide (DMF) was chosen as the "good" solvent for perovskite precursors, and toluene was used as the "bad" solvent. As seen for other tin-based perovskites, 2D tin bromide perovskites often suffer from oxidation under ultraviolet excitation.[7a, 15] To address this issue, we tuned their structure with acidic C-H proton donors such as chloroform (CFM, $CHCl_3$) and dichloromethane (DCM, $CH_2Cl_2$). We note that DCM is often employed as a solvent to wash low-dimensional perovskite crystals or protonated amine precursors, while it would probably form hydrogen

bonds within perovskite lattices and improve crystallinity and thus PL intensity (**Table 1**).[7a, 8c, 16] Meanwhile, hydrogen bonds that form between the perovskite lattice and the introduced C-H protons could, and indeed do, influence their overall PL performance. As a result, the $ODASnBr_4$ perovskite microcrystals showed greatly improved PLQYs approaching 90% with adjustable PL peaks from 570 nm to 608 nm through regulating the amount of the molecular dopants CFM and DCM. Furthermore, they retained stable PL emission under a continuous ultraviolet irradiation, with less than 10% loss in intensity over 6 hours. In contrast, neither tetrachloromethane nor bromoform triggered similar effects, which shows that the hydrogen bond formed between the C-H protons and the $[SnBr_6]^{4-}$ octahedra is the prerequisite for this doping strategy, rather than simply the polarity of the C-Cl bond.

**Table 1.** Comparison of PL characteristics of selected lead-free metal halide perovskites

| Materials | Use of small molecules | $\tau_{avg.}$ (μs) | PL peak (nm) | $T_{90}$ (min) | PLQY (%) | Ref. |
|---|---|---|---|---|---|---|
| $(C_4N_2H_{14}Br)_4SnBr_6$ | DCM | - | ~ 560 | - | - | [7a] |
| $(ODA)Sn_2I_6$ | DCM | 1.11 | 631 | - | 36 | [8c] |
| $(C_8H_{14}N_2)_2SnBr_6$ | - | 1.04 | 507 | - | 36 | [8b] |
| $[(PEA)_4SnBr_6][(PEA)Br]_2[CCl_2H_2]_2$ | DCM | 2.7 | 566 | < 10 | 89.5 | [16a] |
| $(C_9NH_{20})_2SnBr_4$ | - | 6.5 | 695 | 60 | 46 | [17] |
| $Bmpip_2SnBr_4$ | - | 4 | 666 | - | 75 | [18] |
| $(C_4N_2H_{14}Br)_4SnBr_3I_3$ | DCM | 0.7 | 582 | > 60 | 85 | [16b] |
| $(C_4N_2H_{14}Br)_4SnBr_6$ | DCM | 2.2 | 570 | - | 95 | [19] |
| $(C_4H_{14}N_2)_2In_2Br_{10}$ | - | 3.2 | 670 | - | 3 | [20] |
| $ODASnBr_4$ | DCM | >2.9 | 592-608 | 100 | 83±4 | **This work** |
| | Chloroform | >2.4 | 570-598 | 400 | 88±4 | |

## Results and Discussion

Once a 20 μl DMF/perovskite precursor solution droplet was exposed to 1 ml of the bad solvent toluene (feed volume ratio between DMF and toluene, FVR: 2%), the $ODASnBr_4$[2%] perovskite phase would form rapidly, where each of the octahedra slabs is connected through hydrogen bonds by the protonated ODA ligands. Rapid nucleation and growth processes result in the formation of spherical microcrystals, as shown in the scanning electron microscopy (SEM) images in **Figures 1a,b**. In comparison, the same synthetic routine could not generate luminescent materials with monovalent amines. This

suggests a comparatively low formation energy for the DJ structure which could be attributed to the use of the diamine compound with amine groups at either end, which readily stabilized the 2D framework by forming hydrogen bonds with the inorganic octahedra.

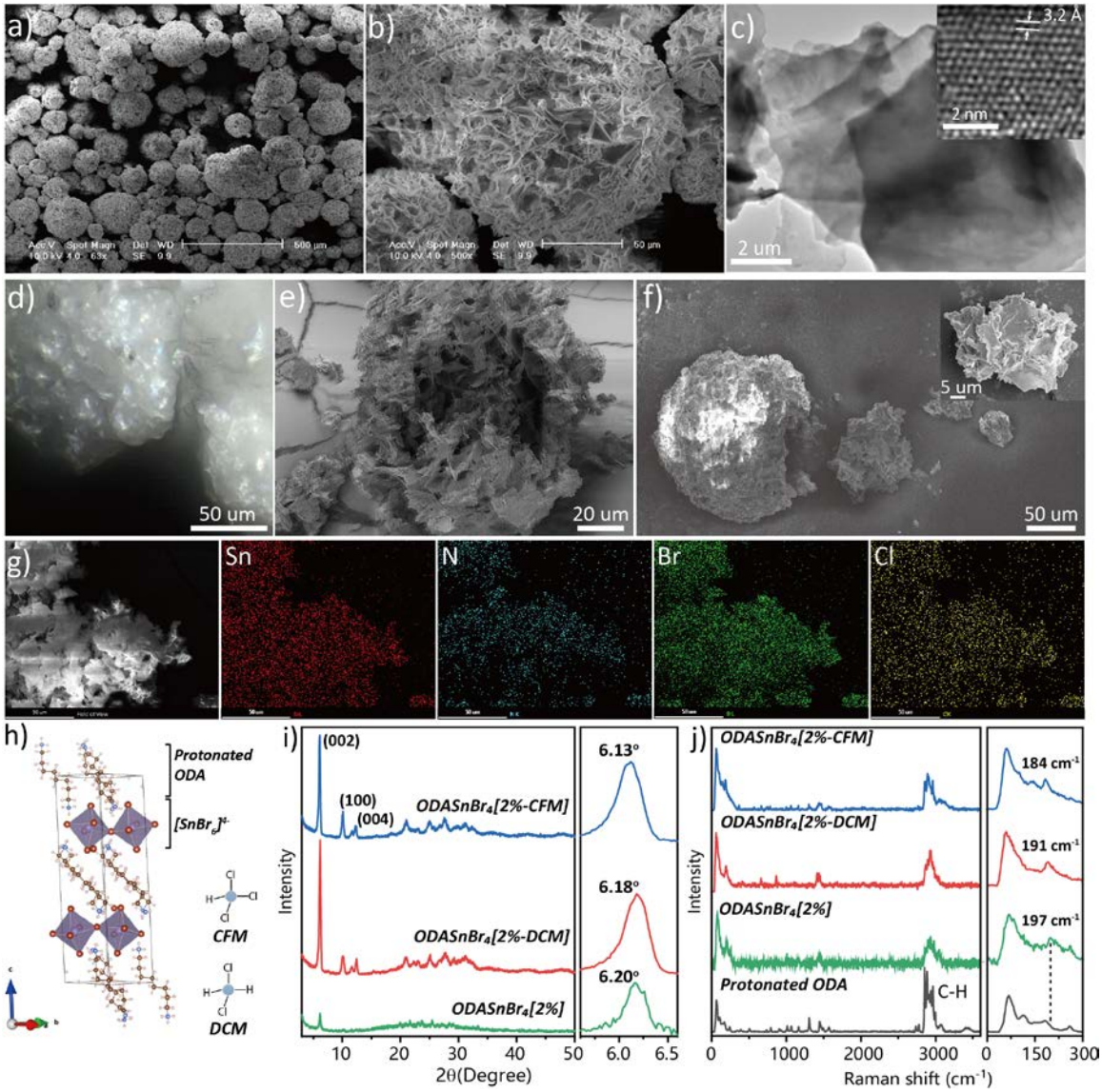


**Figure 1**. (a,b) SEM images, (c) TEM image and (d) confocal microscopy image of the pristine $ODASnBr_4[2\%]$ microcrystals, (e,f) focussed ion beam micro-sectioning images and (g) elemental mapping images of the $ODASnBr_4[2\%\text{-}DCM]$. (h) Structural arrangement of $ODASnBr_4$. (i) Powder XRD spectra and (j) normalized Raman spectra of protonated ODA, pristine $ODASnBr_4[2\%]$, $ODASnBr_4[2\%\text{-}CFM]$ and $ODASnBr_4[2\%\text{-}DCM]$. Inset in (c) is a HRTEM image of a pristine $ODASnBr_4[2\%]$ microcrystal; inset in (f) is a close-up part of the spherical perovskite ablation.

Transmission electron microscopy (TEM) and high-resolution (HR)TEM images in **Figure 1c** show that the pristine ODASnBr$_4$[2%] microcrystals consist of layered perovskites stacking over each other, with a Sn:Br:N atomic ratio of about 1:4:2 according to the TEM-EDS (energy dispersive spectroscopy) mapping data provided in Figure S2. The interplanar spacing of the DJ perovskite observed in the high-resolution TEM images is about 3.2 Å. Furthermore, ODASnBr$_4$[2%] microcrystals were studied by confocal microscopy (**Figure 1d**). The pearlescent appearance of their surface may be attributed to thin-film interference due to the light waves reflected by the upper and lower boundaries of the 2D perovskites, leading to intensification of certain wavelengths while attenuating others. A focused-ion-beam SEM was used to resolve the inner part of the DCM doped perovskite microcrystals (ODASnBr$_4$[2%-DCM]), which maintains the same spherical morphology as the pristine ODASnBr$_4$[2%], consisting of stacked perovskite layers (**Figure 1e, f**). SEM-EDS mapping images provided in **Figure 1g** show the presence of Br, Sn, N and Cl elements in ODASnBr$_4$[2%-DCM], with the atomic ratios of 56%, 14%, 27% and 3%. The occurrence of a few Cl atoms co-localized with a large excess of Br in the doped DJ structure further indicates the formation of hydrogen bonds surrounding the $[SnBr_6]^{4-}$ octahedra.

Crystal structure of ODASnBr$_4$, as determined by single-crystal X-ray diffraction (XRD), is shown in **Figure 1h;** ODASnBr$_4$ exhibits a typical layered DJ-type $n$=1 motive within a centrosymmetric monoclinic $P2_1/c$ space group with lattice parameters of $a$ = 8.2206(17) Å, $b$ = 7.984(3) Å, $c$ = 26.966(6) Å (as listed in Table S1).[21] Powder XRD was used to gain an insight into structural changes induced by the incorporation of small molecules (CFM and DCM) into a pristine ODASnBr$_4$[2%] lattice (**Figure 1i**); from the intensity of diffraction reflections it is evident that both CFM and DCM doping induced enhancement of perovskite ordering and crystallinity compared to pristine sample, but also gave rise to some lattice rearrangements. Le Bail fitting (Figure S3) on the pristine (ODASnBr$_4$[2%]) powder XRD data, as well as on the doped (ODASnBr$_4$[2%-DCM] and ODASnBr$_4$[2%-CFM]) data was performed by using the unit-cell determined from the single crystal analysis as a starting structural model. Pristine ODASnBr$_4$[2%] crystallizes in $P2_1/c$ space group with $a$ = 8.78(1) Å, $b$ = 7.28(3) Å, $c$ = 28.65(2) Å and $\beta$= 93.28(5)°; the observed difference in unit-cell as compared to that obtained from the single crystal

analysis may be attributed to lattice strain and distortions occurring during the rapid nucleation and growth processes. As expected, the most pronounced difference is observed in *c*-direction due to the packing flexibility of ODA cations. When dopant molecules have been introduced, the shift of 002 reflection, from ~6.18° (for $ODASnBr_4$[2%]) to 6.14° and 6.08° for $ODASnBr_4$[2%-DCM] and $ODASnBr_4$[2%-CFM], respectively, was observed. The shift of 00*l* reflections towards the smaller $2\theta$ is the first indication that solvent molecules are indeed incorporated within the perovskite lattice. Refined unit-cells of CFM- and DCM-doped perovskites {$ODASnBr_4$[2%-CFM]: $a$ = 8.79(1) Å, $b$ = 7.35(1) Å, $c$ = 29.02(1) Å and $\beta$= 92.83(4)°; $ODASnBr_4$[2%-DCM]: $a$ = 8.78(1) Å, $b$ = 7.33(3) Å, $c$ = 28.75(1) Å and $\beta$= 92.99(8)°} confirmed that the doping induced the lattice expansion (especially along the *c*-direction) while retaining the typical *n*=1 DJ structure.

Raman spectra further highlighted the observed lattice expansion. As shown in **Figure 1j**, the Raman active mode, $\nu$ ($A_{1g}$), related to the Sn-Br symmetric stretching inside $[SnBr_6]^{4-}$ octahedra,[22] first appeared in the pristine $ODASnBr_4$[2%] at 197 $cm^{-1}$ and then gradually shifted to 191 $cm^{-1}$ for $ODASnBr_4$[2%-DCM], and to 184 $cm^{-1}$ for $ODASnBr_4$[2%-CFM]. This indicates that, consequent to the doping process, the $[SnBr_6]^{4-}$ octahedra were under increased tensile strain resulting in longer Sn-Br bond lengths, and thus a shift to lower resonant frequencies for the Raman active vibrational mode was observed. This suggests that hydrogen bonds formed between the Sn-Br octahedra and the acidic C-H protons caused a certain degree of lattice expansion which benefitted the crystallinity and PL performance.[23] Of note, the pristine $ODASnBr_4$[2%] could gradually precipitate in CFM and DCM solvents but not in tetrachloromethane and bromoform (Figure S4), indicating that the successful formation of C-H…Br hydrogen bonds requires not only proton donors but strong acidic conditions as well, which are not offered in the latter solvents, thereby being incapable of replacing the initial O-H…Br hydrogen bonds. The formation of C-H…Br hydrogen bonds was further verified by performing 1H NMR (nuclear magnetic resonance) measurements. As shown in Figure S5a, active protons in CFM could form C-H…O hydrogen bonds with deuterated DMSO-$d_6$ to generate a resonance signal with a chemical shift at 8.31 ppm, while it shifted to 8.33 ppm and 8.34 ppm for the samples of $ODASnBr_4$[8%-CFM] dissolved in DMSO-$d_6$ with concentrations of 9 mg/ml and 18 mg/ml, respectively. This downfield chemical shift can be attributed to

the formation of C-H…Br hydrogen bonds, corresponding to the reduced electron density and increasing number of de-shielded protons. Similar trends providing evidence on the formation of C-H..Br hydrogen bonds can be derived from $^{1}$H NMR spectra of pure DCM and 20 mg/ml ODASnBr$_4$[2%] and ODASnBr$_4$[2%-DCM] samples, as presented in Figure S5b.

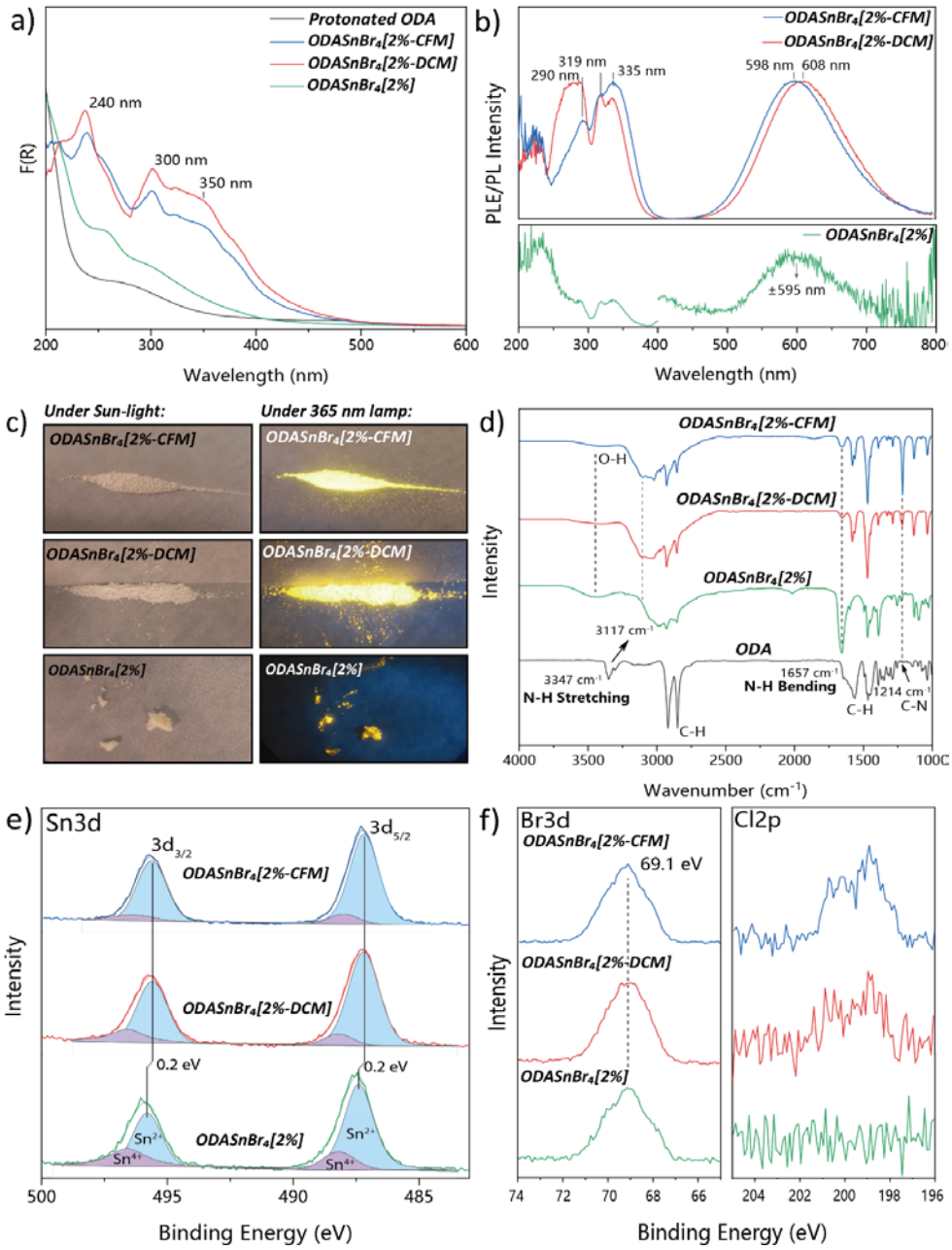


**Figure 2**. Characterisation of pristine ODASnBr$_4$, ODASnBr$_4$[2%-CFM] and ODASnBr$_4$[2%-DCM]. (a) Absorption spectra represented by Kubelka-Munk function, F(R), (b) PL and PLE spectra, (c) photographs taken under sun-light and 365 nm UV lamp illumination, (d) FTIR spectra, and (e,f) XPS spectra of Sn3d, Br3d and Cl2p core levels.

There were no obvious ultraviolet (UV) absorption peaks for the pristine ODASnBr$_4$[2%], as shown in **Figure 2a**, although there were weak features at around 260nm and 300nm. ODASnBr$_4$[2%-DCM] and ODASnBr$_4$[2%-CFM] showed absorption peaks at 240 nm and 300 nm, with a broad shoulder at around 350 nm. **Figure 2b** shows the photoluminescence excitation (PLE) and PL spectra of the three samples. We notice that the pristine ODASnBr$_4$[2%] degraded too fast (within a few minutes) to record the PLQYs once exposed to air and yielded only a weak PL peak (located at ~595 nm) and low-intensity PLE curves, though initial PL was quite bright from direct observation. On the contrary, ODASnBr$_4$[2%-DCM] and ODASnBr$_4$[2%-CFM] microcrystal powders delivered PLQYs of ~90% (excitation wavelength: 335 nm) with 608 nm emission peak and ~85% at 598 nm, respectively, with three obvious apparent PLE peak at 290 nm, 319 nm, and 335 nm. This means that the improved emission originates from the improved crystallinity and improved stability of the DJ perovskite structure. However, if we take into account the absorption features seen in **Figure 2a**, remarked on above, it is most likely that these three PLE peaks are in fact part of one much larger, broad PLE peak with strong dips between the peaks arising from absorption features at 240 nm, 300 nm and 365nm which do not contribute to the PL emission (at 608 nm at least). Even though the doped ODASnBr$_4$ samples had a low PLE intensity at 365 nm which is around 35% of that at 335 nm, they still generated a strong and stable yellow emission under the excitation of a 365 nm UV lamp (**Figure 2c**).

According to the Fourier transform infrared (FTIR) spectra in **Figure 2d**, the N-H stretching vibration of neat ODA shifted from 3347 cm$^{-1}$ to 3117 cm$^{-1}$, indicating the presence of protonated amine when added into DMF with HBr due to the increased effective reduced mass as the N-H group couples via the hydrogen to the octahedral lattice, which leads to a lower vibrational frequency.[9a] After introducing CFM or DCM molecules, the peak at 3117 cm$^{-1}$ solely dominated the FTIR spectrum, while the intensity of the N-H bending vibration at around 1657 cm$^{-1}$ was greatly reduced, pointing out on the occurrence of steric impedance for this mode due to the formation of C-H…Br hydrogen bonds. Further, one could clearly notice the absence of any O-H vibration in both ODASnBr$_4$[2%-CFM] and ODASnBr$_4$[2%-DCM], microcrystals, which illustrates the successful displacement of adsorbed water from HBr by formation of O-H…Br hydrogen bond.

Thermogravimetric analysis and derivative thermogravimetry further showed the existence of the adsorbed water in the pristine ODASnBr$_4$[2%], which appeared as a broad peak at around 100 ºC (Figure S6). In contrast, ODASnBr$_4$[2%-CFM] and ODASnBr$_4$[2%-DCM] showed sharp peaks at 150 ºC and 153 ºC, respectively, due to the cleavage of C-H…Br hydrogen bonds, while broad peaks below 90 ºC correspond to the release of weakly adsorbed CFM and DCM from the perovskite surface. X-ray photoelectron spectroscopy (XPS) measurements demonstrated that the binding energy of nitrogen in all doped samples is 0.1 eV higher than in the pristine ODASnBr$_4$[2%], revealing an improved coordination between the protonated amine and the $[SnBr_6]^{4-}$ octahedral slabs (Figure S7). To some extent, the appearance of the free amine could reflect the interaction between $[SnBr_6]^{4-}$ octahedra and CFM molecules which resulted in the deprotonation of -$NH_2$·HBr from poorly crystalized perovskite lattices and/or protonated ODA. As shown in **Figure 2e**, the binding energy of Sn(II) in both doped samples is 0.2 eV lower than that in the pristine ODASnBr$_4$. The proportion of oxidized Sn(IV) also decreased from 24% (pristine ODASnBr$_4$[2%]) to 16% (ODASnBr$_4$[2%-CFM]) and 11% (ODASnBr$_4$[2%-DCM]).[24] In each case here the Sn(II) contents are given in absolute atomic %. Further, the Br:Sn:N:Cl elemental ratio of the ODASnBr$_4$ microcrystal changed from 57:13:30:0 (pristine ODASnBr$_4$[2%]) to 55:13:27:5 (ODASnBr$_4$[2%-CFM]) and 56:13:29:2 (ODASnBr$_4$[2%-DCM]), which matches well with the element ratios derived from the SEM-EDS data. The presence of the chlorine further suggests the successful incorporation of the molecular dopants CFM and DCM (**Figure 2f**).

It is widely accepted that STEs dominate the radiative recombination process in low-dimensional lead-free perovskites, while their emission maximum position is limited by the depth of the self-trapped state, subject to other band gap modifying factors related to the choices of the A-site ions or halides.[16b] As depicted in Figure S1, the reconfiguration of the upper manifold of the excited state from the free exciton case to the STE arrangement can significantly influence the radiative emission energy. With this in mind, we originally tried to prolong the treatment time and increase the volume of the doping solvents in an attempt to manipulate the STE state to tune the emission wavelength via that mechanism, which however proved to be ineffective. This suggests that the achievable maximum content of dopants is strictly limited by the level of lattice distortions, rather than the

amount of dopant or any extended durations allowed for further dopant uptake. Therefore, we moved to regulate the FVR (x%) between the good and the bad solvent, in an attempt to obtain pristine ODASnBr$_4$[x%] perovskite microcrystals with various levels of lattice distortions providing the opportunity for different exposure levels to C-H proton donors. The FVR was chosen as 2%, 8%, 16%, 30%, 50% and 70%, meaning that 20 µl, 80 µl, 160 µl, 300 µl, 500 µl and 700 µl precursor mixture was injected into 1 ml toluene, respectively. After 8 min, the precipitates, named "pristine lattice [x%]" (e.g. ODASnBr$_4$[x%]), were collected by centrifuging at 2000 rpm for 2 min and transferred into 2 ml CFM or DCM for 30 min. In this way, as shown in **Figures 3a,b**, PL peaks of the resulting samples could be fine-tuned, according to the amount of lattice distortion imparted to the pristine forms. The emission spectra, under an excitation wavelength of 335 nm, showed a shift in the PL peak intensities across a window of 28 nm (from 608 nm to 592 nm, PLQYs: 83 ± 4%) and 16 nm (from 598 nm to 570 nm, PLQYs: 88 ± 4%) for ODASnBr$_4$[x%-DCM] and ODASnBr$_4$[x%-CFM], respectively. Here the sample nomenclature has CFM or DCM added to denote the molecular dopant used to treat the distorted pristine forms. But note that the x% token denotes the FVR of good and bad solvent used to obtain the distorted pristine lattices, and does not indicate any feed ratio for DCM or CFM. These dopants are administered to saturate the available and accessible sites furnished via the lattice distortions. The PLE spectra show the same apparent PLE peaks at 290 nm, 319 nm and 335 nm, again the features shown in the absorption spectra of Figure 2a are most likely introducing the dips between these apparent peaks and distorting an otherwise broader, less complex PLE peak. The distortion of the peak by these absorptions makes it hard to accurately locate the true position of the PLE maximum, though for the whole set of doped and pristine samples the peaks would appear to lie in the 280 nm to 340 nm range. This indicates that the Stokes shifts are certainly over 300 nm, and this is a very large fraction of the emission wavelengths, a feature strongly characteristic of STEs. We note that the morphology of the doped ODASnBr$_4$ materials gradually changed to smaller and more flat microcrystals with increases in the FVR (Figure S8). Meanwhile, the ODASnBr$_4$ microcrystals with FVR over 50% tended to be better maintained in suspension, further suggesting that smaller microcrystals had been formed (Figure S9a). We have also observed a huge reduction in the PLE intensity at 290 nm for the ODASnBr$_4$[x%-CFM]

with a strong absorption peak at 240 nm (Figure S9b), in comparison with $ODASnBr_4$[x%-DCM] (Figure S10 (a-d)). For the CFM doped material, the PLE peaks appear (taking into account the forementioned absorption features) to be sharper and shifted further to the red than for their corresponding DCM doped counterparts. These observations suggest an improved relaxation channel for excitons within the conduction band and more limited nonradiative recombination centers after incorporating DCM. At the same time, the PL peaks of the pristine $ODASnBr_4$[x%] microcrystals remained almost fixed with a relatively narrower full width at half maximum (FWHM) of about 124 nm (Figure S9c).

**Figure 3c** shows an overview of the emission performance of $ODASnBr_4$[x%-CFM] and $ODASnBr_4$[x%-DCM] including the evolution of the PL maxima and their similar FWHMs of about 135 nm, further demonstrating that the radiative recombination process arise from STEs and that more lattice distortions were involved after molecular doping.[25] The average PL lifetimes ($\tau_{avg}$) of the $ODASnBr_4$[x%] with different dopants were evaluated following the previously reported procedure.[26] $ODASnBr_4$[x%-CFM] had shorter average PL lifetimes (2.39-2.83 μs) while $ODASnBr_4$[x%-DCM] had slightly longer average PL lifetimes (3.10-3.17 μs). The decays of both sets of materials were better fitted by double-exponential PL decay curves with a weak (few %) second decay term. The DCM based samples showed noticeably less variation in the average PL lifetime compared with the CFM doped materials.

Powder XRD patterns in **Figure 3e,f** demonstrate that both $ODASnBr_4$[x%-CFM] and $ODASnBr_4$[x%-DCM] underwent FVR-dependent lattice dilations. The XRD peak corresponding to the (002) plane of the DJ-phase $ODASnBr_4$ shifted by 1.6° and 0.8° toward lower 2θ angles with the incremental FVR for $ODASnBr_4$[x%-CFM] and $ODASnBr_4$[x%-DCM], respectively. The dilation could be attributed to the formation of C-H…Br hydrogen bonds which stretched the $[SnBr_6]^{4-}$ octahedron lattice and in turn modified the STE depth thereby tuning the emissions. The SEM-EDS data in Figure S9d demonstrate that both $ODASnBr_4$[x%-CFM] and $ODASnBr_4$[x%-DCM] perovskite microcrystals could still maintain their typical DJ structure after incorporating different amount of small molecular dopants. Based upon the proportions of chlorine present in the samples, the overall C-H donor percentages present in $ODASnBr_4$[x%-DCM] are found to be slightly higher than the corresponding cases for $ODASnBr_4$[x%-CFM], which could

further indicate that the over-stretched lattices in the latter samples stem from the higher polarity of the CFM C-H protons.

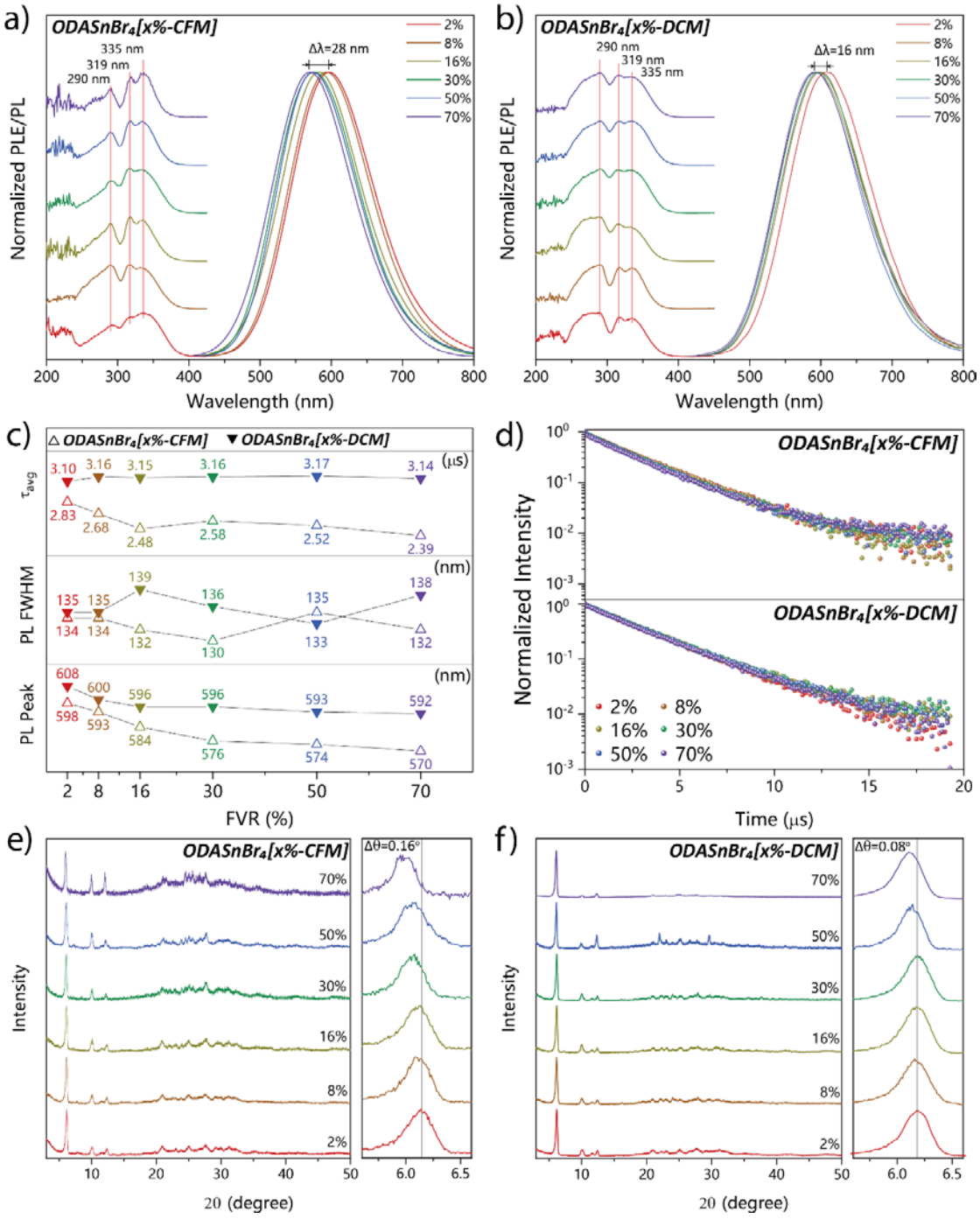


**Figure 3**. PL and PLE spectra of (a) ODASnBr$_4$[x%-CFM] and (b) ODASnBr$_4$[x%-DCM] with various precursor FVRs (x%). (c) Trends for the PL peak position, FWHM and average PL lifetime as a function of FVR and (d) PL decay curves of these two sets of samples. Powder XRD patterns of (e) ODASnBr$_4$[x%-CFM] and (f) ODASnBr$_4$[x%-DCM] with different FVRs.

Comparative temperature-dependent measurements were conducted, based on ODASnBr$_4$[16%-DCM] and ODASnBr$_4$[70%-CFM], these being selected due to their similar doping content of C-H proton donors at around 3.1%. As summarized in **Figure 4a**, during the heating process from 77 K to 298 K, ODASnBr$_4$[70%-CFM] experienced a 9.3% reduction of its initial average PL lifetime, while ODASnBr$_4$[16%-DCM] microcrystals displayed a 7.5% reduction of its initial average PL lifetime. Further, red-shifted PLE spectra with fixed apparent peaks at 290 nm, 319 nm and 335 nm were observed without the emergence of free excitons (Figure S10). As already mentioned, these peaks are most likely the result of the absorption peaks observed (e.g. Figure 8c) which do not themselves contribute to the emission process. In the temperature range from 160 K to 240 K the PL intensity stopped decreasing. This could suggest the occurrence of a thermal activation for radiative recombination which might relate to a possible (e.g. plastic crystal type) phase transition of the entrapped molecular dopants. In contrast, for the temperatures above 240 K, both samples' PL intensities started to drop again and the PL spectra became broader, which marks an increased electron-phonon coupling as discussed further below. Importantly, even when approaching room temperature, ODASnBr$_4$[16%-DCM] and ODASnBr$_4$[70%-CFM] could still maintain 82% and 73% of their initial low temperature PL intensities, respectively. Other low-dimensional perovskites have been reported declines to less than 60% of their initial PL intensity over the same temperature range (Table 1).[8c, 27] The difference may be attributed to the high exciton binding energy ($E_B$) for STEs in the single-layered DJ perovskites. Specifically, $E_B$ can be calculated from the temperature-dependent PL intensity *I(T)* using the Arrhenius equation:[27b]

$$I(T) = \frac{I_0}{1 + Ae^{-E_B/k_BT}} \quad (1)$$

where $I_0$ is the PL intensity at 0 K, $k_B$ is the Boltzmann constant, $A$ is a pre-exponential constant factor. The $E_B$ values for ODASnBr$_4$[70%-CFM] and ODASnBr$_4$[16%-DCM] at 298 K are calculated to be 61.3 meV and 70.7 meV, respectively (Figure S11), lower than the value reported for other low-dimensional metal halide perovskites (> 120 meV) which contributes to the exciton dissociation.[28] We note that the fitting process we used here excluded the data points at 120 K, 160 K and 200 K where there was a clear deviation from the simple trend predicted by equation (1). Similar, but weaker, features also appeared in

Figure 3d in Ref. [22b] and Figure 3c in Ref. [11b]. Larger deviations in our case could relate to a possible phase transition of the entrapped molecular dopants.

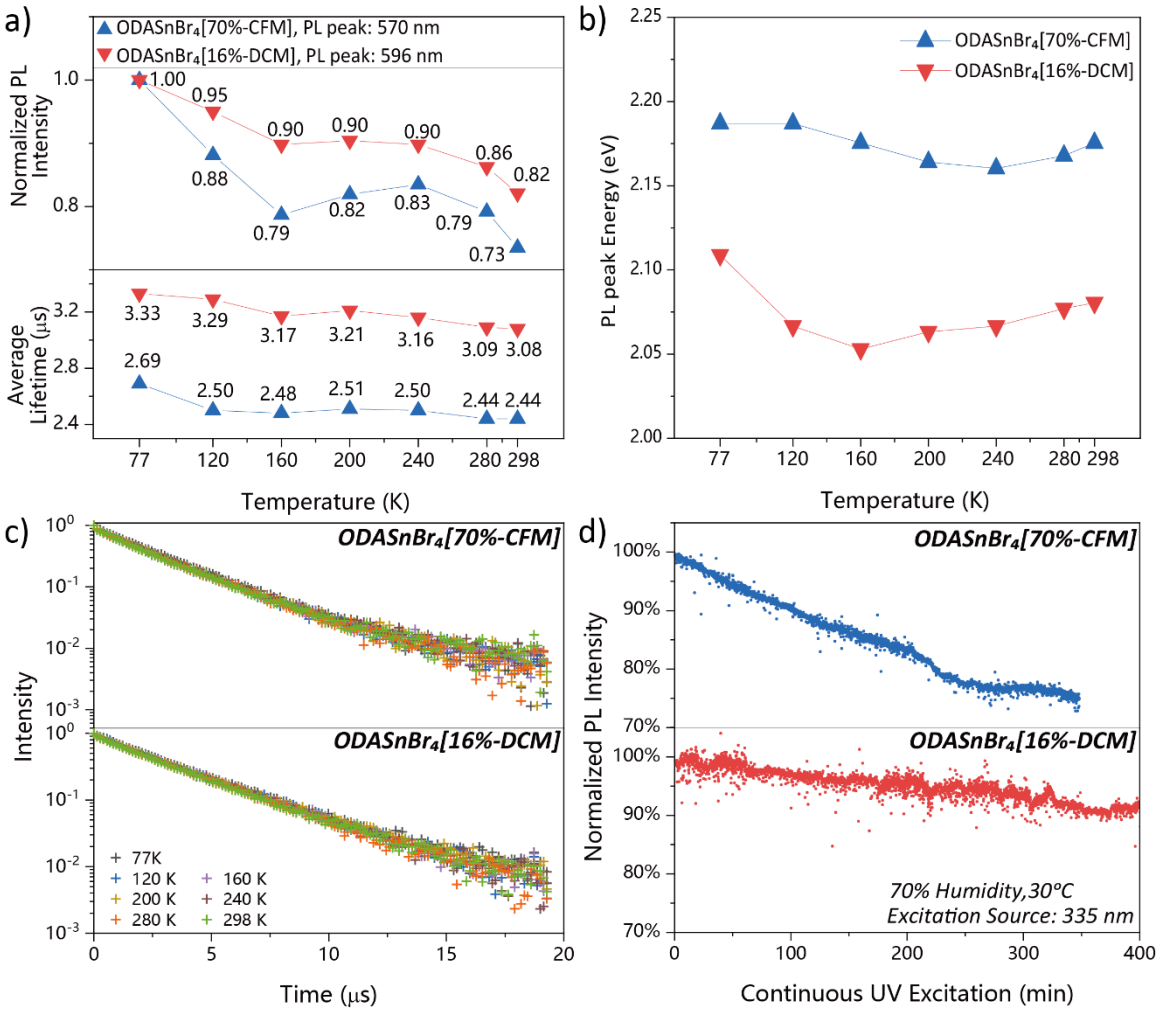


**Figure 4**. (a) Temperature-dependent average PL lifetime and PL intensity evolution (normalized *vs.* starting intensities), (b) PL peak energy evolution, (c) PL decay curves of $ODASnBr_4$[70%-CFM] and $ODASnBr_4$[16%-DCM] and (d) evaluation of their PL stability under continuous 335 nm UV excitation (~ 300 µW/cm$^2$, temperature 30°C, relative humidity 70%).

**Figure 4b** shows the evolution of the energies of the PL maxima upon increasing temperature, which exhibits concave curves resulting from the combined contributions of electron-phonon interactions and the thermal dilatation of the lattice assuming a linear relationship between lattice constant and temperature.[29] Thermal expansion could decrease the interaction between the Sn-5s and Br-4p orbitals, leading to a reduction of the valence band maximum of the $ODASnBr_4$ microcrystals and in turn an increase of the

bandgap, resulting in the blue shift of the PL spectra with increasing temperature.[30] Therefore, the linear increase in the PL peak energy can be attributed to the dominance of thermal expansion above 160 K for ODASnB $r_4$[16%-DCM] (0.20 meV/K), and above 240 K for ODASnBr$_4$[70%-CFM] (0.26 meV/K), during which the variation in the electron-phonon coupling is negligible. In contrast, the electron-phonon coupling dominates at lower temperatures, leading to the red-shift in the PL in that range. To evaluate the extent of the electron-phonon coupling, the temperature-dependence of the PL FWHM (Figure S12) was fitted based on the following equation:[31]

$$\text{FWHM}\,(T) = 2.36\sqrt{S}\hbar\omega_{phonon}\sqrt{\coth\left(\frac{\hbar\omega_{phonon}}{2k_BT}\right)} \quad (2)$$

where $\hbar\omega_{phonon}$ is the phonon frequency ($\hbar$, reduced Plank constant), $S$ is the electron-phonon coupling parameter (Huang-Rhys factor), and $k_B$ is the Boltzmann constant. It should be noted that Luo et al. in Ref. [26] gave Stadler et al.'s expression for the FWHM (T) dependence (our equation (2)) with a typographical error: the hyperbolic coth form as shown here is the correct version to use.[32] S and $\hbar\omega_{phonon}$ for ODASnBr$_4$[16%-DCM] were found to be 27.5 and 23.9 meV, respectively, while ODASnBr$_4$[70%-CFM] showed a comparable Huang-Rhys factor of 26.0 and $\hbar\omega_{phonon}$ of 26.7 meV, revealing strong electron-phonon coupling (typically corresponding to S > 10) in the DJ perovskite matrix modified by each of the small molecular proton donors. It is notable that the latter sample was again fitted without including the same three temperature points as above (120 K, 160 K and 200 K) so as avoiding the range where a clear deviation from equation (2) was seen. However, if those three data points are included, the poorer overall fit still predicts an S factor of around 20 indicating strong electron phonon coupling nonetheless.

Additional insights into the exciton recombination mechanism could be derived from the temperature-dependent time-resolved PL decays (**Figure 4c**). The ODASnBr$_4$[16%-DCM] sample maintained single-exponential decays in the broad temperature range of 77 K to 298 K, while PL decays of ODASnBr$_4$[70%-CFM] were slightly bi-exponential in that temperature range. In both cases the PL average lifetimes shortened by 0.25 μs over the course of the heating process. It is worth noting that in both cases the average PL lifetime/ temperature curves exhibited weak, broad local maxima in the region of around 200 K. This weak feature may again be an evidence of an underlying

weak phase transition; it points out on gradually activated thermal motion of the dopants which slightly impedes the radiative recombination of excitons, thus elevating the PL lifetimes to some extent, in that temperature range.

While the pristine ODASnBr$_4$[x%] perovskite microcrystals suffered from a fast degradation of their PL intensity in air, presumably due to oxidation, both types of doped samples showed greatly improved stability towards UV excitation and the presence of oxygen, as shown in **Figure 4d**. ODASnBr$_4$[70%-CFM] perovskite could maintain over 90% of its original intensity after 100 min ($T_{90}$) continuous UV excitation at a wavelength of 335 nm, performed at a temperature of 30 ºC and relative humidity of 70%. The $T_{90}$ value was even higher (400 min) for ODASnBr$_4$[16%-DCM] under the same conditions.

## Conclusions

We synthesized lead-free ODASnBr$_4$ DJ perovskite microcrystals with limited PL stability, which could be greatly improved, and obtained PLQY approaching 90% by doping small molecule proton donors such as CFM and DCM into the perovskite lattice. The process is facilitated by controlling the distortion of the lattice prior to doping in order to allow ready access of the dopants in a post synthesis step. The dopant molecules CFM and DCM that were used here are the same ones that are also frequently used to remove organic impurities from low-dimensional perovskite crystals during washing procedures as reported in the literature. The PL peak position of perovskites could be shifted through fine-tuning ODASnBr$_4$ microcrystals for forming C-H…Br hydrogen bonds, with emission peaks ranging from 608 nm to 592 nm for ODASnBr$_4$[DCM] and from 598 nm to 570 nm for ODASnBr$_4$[CFM], while maintaining high PLQYs (83 - 88%). The ODASnBr$_4$[16%-DCM] perovskite microcrystals preserved over 90% of the initial PL intensity under a continuous UV irradiation for 400 min in air. Further, the similar variation trends in phonon broadening of the PL emission, temperature-dependent PL intensity and the corresponding PL lifetime could bring some insight into the interaction between the dopants and the lattice as it expands during heating cycles and that may imply some form of underlying phase transition warranting further investigations. The small molecule doping strategy introduced in this work has a great potential to improve the performance and stability of tin-based

perovskite materials and promote their practical applications. Our study contributes to the development of stable, strongly emitting lead-free DJ perovskite materials.

## Supporting Information

Supporting Information is available from the Wiley Online Library or from the author.

## Acknowledgments

We acknowledge financial support from the Research Grant Council of Hong Kong (GRF 17301520 and CRF C7035-20G), the joint project of the National Science Foundation of China / Research Grant Council of Hong Kong (N_CityU108/17), the Croucher Foundation of Hong Kong, and the "Research Cooperability" Program of the Croatian Science Foundation funded by the EU *via* European Social Fund under the Operational Program "Efficient Human Resources 2014-2020".

Received: ((will be filled in by the editorial staff))
Revised: ((will be filled in by the editorial staff))
Published online: ((will be filled in by the editorial staff))

## References


[1] a) S. Yang, S. Chen, E. Mosconi, Y. Fang, X. Xiao, C. Wang, Y. Zhou, Z. Yu, J. Zhao, Y. Gao, F. De Angelis, J. Huang, *Science* **2019**, *365*, 473-478; b) S. Wang, C. Bi, A. Portniagin, J. Yuan, J. Ning, X. Xiao, X. Zhang, Y. Y. Li, S. V. Kershaw, J. Tian, A. L. Rogach, *ACS Energy Lett.* **2020**, 2401-2410.

[2] N. Wang, L. Cheng, R. Ge, S. Zhang, Y. Miao, W. Zou, C. Yi, Y. Sun, Y. Cao, R. Yang, Y. Wei, Q. Guo, Y. Ke, M. Yu, Y. Jin, Y. Liu, Q. Ding, D. Di, L. Yang, G. Xing, H. Tian, C. Jin, F. Gao, R. H. Friend, J. Wang, W. Huang, *Nat. Photon.* **2016**, *10*, 699-704.

[3] N. Zhang, Y. Fan, K. Wang, Z. Gu, Y. Wang, L. Ge, S. Xiao, Q. Song, *Nat. Commun.* **2019**, *10*, 1770.

[4] S. Han, Y. Yao, X. Liu, B. Li, C. Ji, Z. Sun, M. Hong, J. Luo, *Small* **2019**, e1901194.

[5] W. H. Qian, X. F. Cheng, Y. Y. Zhao, J. Zhou, J. H. He, H. Li, Q. F. Xu, N. J. Li, D. Y. Chen, J. M. Lu, *Adv. Mater.* **2019**, *31*, e1806424.

[6] S. Hou, Y. Guo, Y. Tang, Q. Quan, *ACS Appl. Mater. Inter.* **2017**, *9*, 18417-18422.

[7] a) C. Zhou, Y. Tian, M. Wang, A. Rose, T. Besara, N. K. Doyle, Z. Yuan, J. C. Wang, R. Clark, Y. Hu, T. Siegrist, S. Lin, B. Ma, *Angew Chem. Int. Ed.* **2017**, *56*, 9018-9022; b) Y. Li, J. V. Milic, A. Ummadisingu, J. Y. Seo, J. H. Im, H. S. Kim, Y. Liu, M. I. Dar, S. M. Zakeeruddin, P. Wang, A. Hagfeldt, M. Gratzel, *Nano Lett.* **2019**, *19*, 150-157; c) L. Mao, C. C. Stoumpos, M. G. Kanatzidis, *J. Am. Chem. Soc.* **2018**.

[8] a) M. Chen, M.-G. Ju, M. Hu, Z. Dai, Y. Hu, Y. Rong, H. Han, X. C. Zeng, Y. Zhou, N. P. Padture, *ACS Energy Lett.* **2018**, *4*, 276-277; b) B. Su, G. Song, M. S. Molokeev, Z. Lin, Z. Xia, *Inorg. Chem.* **2020**, *59*, 9962-9968; c) I. Spanopoulos, I. Hadar, W. Ke, P. Guo, S. Sidhik, M. Kepenekian, J. Even, A. D. Mohite, R. D. Schaller, M. G. Kanatzidis, *J. Am. Chem. Soc.* **2020**, *142*, 9028-9038.

[9] a) X. Zhang, C. Wang, Y. Zhang, X. Zhang, S. Wang, M. Lu, H. Cui, S. V. Kershaw, W. W. Yu, A. L. Rogach, *ACS Energy Lett.* **2018**, *4*, 242-248; b) L. Mao, W. Ke, L. Pedesseau, Y. Wu, C. Katan, J. Even, M. R. Wasielewski, C. C. Stoumpos, M. G. Kanatzidis, *J. Am. Chem. Soc.* **2018**, *140*, 3775-3783; c) E. I. Marchenko, S. A. Fateev, A. A. Petrov, V. V. Korolev, A. Mitrofanov, A. V. Petrov, E. A. Goodilin, A. B. Tarasov, *Chem. Mater.* **2020**, *32*, 7383-7388.

[10] Z. Chen, Y. Guo, E. Wertz, J. Shi, *Adv. Mater.* **2019**, *31*, e1803514.

[11] a) R. T. Williams, K. S. Song, *J. Phys. Chem. Solids* **1990**, *51*, 679-716; b) A. Yangui, D. Garrot, J. S. Lauret, A. Lusson, G. Bouchez, E. Deleporte, S. Pillet, E. E. Bendeif, M. Castro, S. Triki, Y. Abid, K. Boukheddaden, *J. Phys. Chem. C* **2015**, *119*, 23638-23647; c) G. Zhou, B. Su, J. Huang, Q. Zhang, Z. Xia, *Mater. Sci. Eng. R Rep.* **2020**, *141*; d) M. Li, Z. Xia, *Chem. Soc. Rev.* **2021**.

[12] S. Ahmad, P. Fu, S. Yu, Q. Yang, X. Liu, X. Wang, X. Wang, X. Guo, C. Li, *Joule* **2019**, *3*, 794-806.

[13] G. Zhou, X. Jiang, M. Molokeev, Z. Lin, J. Zhao, J. Wang, Z. Xia, *Chem. Mater.* **2019**, *31*, 5788-5795.

[14] a) F. Zhang, H. Zhong, C. Chen, X. G. Wu, X. Hu, H. Huang, J. Han, B. Zou, Y. Dong, *ACS Nano* **2015**, *9*, 4533-4542; b) Z. Lian, Q. Yan, T. Gao, J. Ding, Q. Lv, C. Ning, Q. Li, J. L. Sun, *J. Am. Chem. Soc.* **2016**, *138*, 9409-9412.

[15] T. Leijtens, R. Prasanna, A. Gold-Parker, M. F. Toney, M. D. McGehee, *ACS Energy Lett.* **2017**, *2*, 2159-2165.

[16] a) L.-J. Xu, H. Lin, S. Lee, C. Zhou, M. Worku, M. Chaaban, Q. He, A. Plaviak, X. Lin, B. Chen, M.-H. Du, B. Ma, *Chem. Mater.* **2020**, *32*, 4692-4698; b) C. Zhou, Y. Tian, Z. Yuan, H. Lin, B. Chen, R. Clark, T. Dilbeck, Y. Zhou, J. Hurley, J. Neu, T. Besara, T. Siegrist, P. Djurovich, B. Ma, *ACS Appl. Mater. Interfaces* **2017**, *9*, 44579-44583.

[17] C. Zhou, H. Lin, H. Shi, Y. Tian, C. Pak, M. Shatruk, Y. Zhou, P. Djurovich, M. H. Du, B. Ma, *Angew Chem. Int. Ed.* **2018**, *57*, 1021-1024.

[18] V. Morad, Y. Shynkarenko, S. Yakunin, A. Brumberg, R. D. Schaller, M. V. Kovalenko, *J. Am. Chem. Soc.* **2019**, *141*, 9764-9768.

[19] C. Zhou, H. Lin, Y. Tian, Z. Yuan, R. Clark, B. Chen, L. J. van de Burgt, J. C. Wang, Y. Zhou, K. Hanson, Q. J. Meisner, J. Neu, T. Besara, T. Siegrist, E. Lambers, P. Djurovich, B. Ma, *Chem. Sci.* **2018**, *9*, 586-593.

[20] L. Zhou, J. F. Liao, Z. G. Huang, J. H. Wei, X. D. Wang, H. Y. Chen, D. B. Kuang, *Angew Chem. Int. Ed.* **2019**, *58*, 15435-15440.

[21] G. M. Sheldrick, *Acta Crystallogr. A Found. Adv.* **2015**, *71*, 3-8.

[22] a) G. Yuan, S. Huang, J. Niu, S. Qin, X. Wu, H. Ding, A. Lu, *Solid State Commun.* **2018**, *275*, 68-72; b) A. Mhiri, F. Krichen, A. Oueslati, J. Lhoste, F. Goutenoire, M. Gargouri, A. Bulou, *J. Alloys Compd.* **2019**, *772*, 546-556.

[23] F. H. Allen, P. A. Wood, P. T. Galek, *Acta Crystallogr. B Struct. Sci. Cryst. Eng. Mater.* **2013**, *69*, 379-388.

[24] H. Liang, F. Yuan, A. Johnston, C. Gao, H. Choubisa, Y. Gao, Y. K. Wang, L. K. Sagar, B. Sun, P. Li, G. Bappi, B. Chen, J. Li, Y. Wang, Y. Dong, D. Ma, Y. Gao, Y. Liu, M. Yuan, M. I. Saidaminov, S. Hoogland, Z. H. Lu, E. H. Sargent, *Adv. Sci.* **2020**, *7*, 1903213.

[25] A. M. Stoneham, J. Gavartin, A. L. Shluger, A. V. Kimmel, D. M. Ramo, H. M. Rønnow, G. Aeppli, C. Renner, *Journal of Physics: Condensed Matter* **2007**, *19*.

[26] S. Wang, Y. Wang, Y. Zhang, X. Zhang, X. Shen, X. Zhuang, P. Lu, W. W. Yu, S. V. Kershaw, A. L. Rogach, *J. Phys. Chem. Lett.* **2019**, *10*, 90-96.

[27] a) N. Mondal, R. Naphade, X. Zhou, Y. Zheng, K. Lee, I. Gereige, A. Al-Saggaf, O. M. Bakr, O. F. Mohammed, Y. N. Gartstein, A. V. Malko, *J. Phys. Chem. Lett.* **2020**, *11*, 1112-1119; b) B. Luo, D. Liang, S. Sun, Y. Xiao, X. Lian, X. Li, M. D. Li, X. C. Huang, J. Z. Zhang, *J. Phys. Chem. Lett.* **2020**, *11*, 199-205.

[28] a) J. Yu, J. Kong, W. Hao, X. Guo, H. He, W. R. Leow, Z. Liu, P. Cai, G. Qian, S. Li, X. Chen, X. Chen, *Adv. Mater.* **2019**, *31*, e1806385; b) M. I. Saidaminov, O. F. Mohammed, O. M. Bakr, *ACS Energy Lett.* **2017**, *2*, 889-896; c) S. Yu, Y. Yan, M. Abdellah, T. Pullerits, K. Zheng, Z. Liang, *Small* **2019**, *15*, e1905081.

[29] a) Q. Xu, W. Shao, X. Zhang, J. Liu, X. Ouyang, X. Tang, W. Jia, *J Alloys Compd.* **2019**, *792*, 185-190; b) Y. P. Varshni, *Physica* **1967**, *34*, 149-154.

[30] L.-y. Huang, W. R. L. Lambrecht, *Physical Review B* **2013**, *88*.

[31] J. Luo, X. Wang, S. Li, J. Liu, Y. Guo, G. Niu, L. Yao, Y. Fu, L. Gao, Q. Dong, C. Zhao, M. Leng, F. Ma, W. Liang, L. Wang, S. Jin, J. Han, L. Zhang, J. Etheridge, J. Wang, Y. Yan, E. H. Sargent, J. Tang, *Nature* **2018**, *563*, 541-545.

[32] W. Stadler, D. M. Hofmann, H. C. Alt, T. Muschik, B. K. Meyer, E. Weigel, G. Muller-Vogt, M. Salk, E. Rupp, K. W. Benz, *Phys. Rev. B* **1995**, *51*, 10619-10630.

**TOC Entry**

Small molecule dopants containing acidic C-H proton donors, such as chloroform and dichloromethane stretch octahedron slabs in Dion-Jacobson (DJ) tin bromide perovskites by forming hydrogen bonds, which results in their enhanced stability, photoluminescence quantum yields approaching 90%, and tunable emission maxima.